

See discussions, stats, and author profiles for this publication at: <https://www.researchgate.net/publication/263954074>

Compartment Modeling and Flow Characterization in Nonisothermal Underground Coal Gasification Cavities

ARTICLE in INDUSTRIAL & ENGINEERING CHEMISTRY RESEARCH · MARCH 2012

Impact Factor: 2.59 · DOI: 10.1021/ie200410u

READS

22

7 AUTHORS, INCLUDING:



Sateesh Daggupati

Reliance Industries Limited

11 PUBLICATIONS 70 CITATIONS

SEE PROFILE



Sanjay Madhusudan Mahajani

Indian Institute of Technology Bombay

123 PUBLICATIONS 1,392 CITATIONS

SEE PROFILE



Anuradda Ganesh

indian institute of technology, Bombay

44 PUBLICATIONS 1,359 CITATIONS

SEE PROFILE



Preeti Aghalayam

Indian Institute of Technology Madras

37 PUBLICATIONS 636 CITATIONS

SEE PROFILE

Compartment Modeling and Flow Characterization in Nonisothermal Underground Coal Gasification Cavities

Sateesh Daggupati,[†] Ramesh N. Mandapati,[†] Sanjay M. Mahajani,[†] Anuradda Ganesh,[‡] A. K. Pal,[§] Rakesh K. Sharma,[§] and Preeti Aghalayam^{*,†}

[†]Department of Chemical Engineering, IIT Bombay, Powai, Mumbai-400076, India

[‡]Energy Science and Engineering, IIT Bombay, Powai, Mumbai-400076, India

[§]UCG Group, IRS, ONGC, Chandkheda, Ahmedabad-380005, Gujarat, India

ABSTRACT: Characterization of reactant gas flow patterns in the underground coal gasification (UCG) cavity is important, because the flow is highly nonideal and likely to influence the quality of the product gas. In our earlier work [Daggupati et al., *Energy* 2010, 35, 2374–2386], we have demonstrated a computational fluid dynamics (CFD)-based modeling approach to analyze the flow patterns in the cavity. A compartment model (network of ideal reactors) for the UCG cavity was developed based on the CFD simulation results. These studies were performed assuming that the UCG cavity is isothermal. In reality, large temperature gradients may prevail under certain conditions and, in turn, may influence the flow patterns. In this work, we consider different possible nonisothermal scenarios in the UCG cavity and propose a simplified compartment modeling strategy to reduce the computational burden. We also examine the effect of various operating and design parameters such as coal spalling, feed flow rate, feed temperature, and orientation of the inlet nozzle. All these effects are quantified by determining the corresponding compartment model parameters. The sensitivity of the compartment model parameters, with respect to the changes in various conditions, is studied. Furthermore, we validate the compartment modeling approach by comparing predicted conversions for a water-gas shift reaction with that of reaction-enabled CFD simulations under nonisothermal conditions. The results presented here provide adequate insight into the UCG process and can be conveniently used in the development of a computationally inexpensive phenomenological process model for the complex UCG process.

1. INTRODUCTION

Coal is a major fossil fuel with total proven worldwide reserves of 827 billion tonnes.¹ It provides 29.4% of the global primary energy needs and generates ~40% of the world's electricity.^{1,2} In India, coal typically has high ash content (35%–50%) and ~37% of the total coal reserves are at depths of 300–1200 m.³ The extraction of these deep-seated coal reserves with current mining techniques may not be possible, because of the greater depths, poor coal quality, and cost of mining. Underground Coal Gasification (UCG) is a promising alternate technology that will enable the utilization of the vast coal reserves in an environment friendly manner. Increasing energy demands, depletion of oil and gas resources, and the threat of global climate change have led to a growing interest in UCG. UCG eliminates many of the health, safety, and environmental problems that are associated with deep coal mining and handling of coal on the surface for various applications. The UCG product gas, called syngas, is a mixture of CO, H₂, CH₄, and CO₂ with trace amounts of ethane. Syngas can be utilized for power generation or as a feedstock for the production of chemicals or liquid fuels. In addition, syngas can be processed to remove its CO₂ content before it is provided to the end users. The captured CO₂ can then be stored underground, thereby contributing to climate change mitigation.⁴ Surface subsidence and contamination of surrounding aquifers are the two major issues with UCG, which must be addressed through careful site selection and environment related studies during the pilot-scale tests.

During in situ gasification, an underground cavity is formed due to the reaction between coal and the feed gases (see Figure 1).

The volume of the cavity increases progressively with coal consumption and thermomechanical spalling, if any, from the roof.⁵ As the cavity growth is irregular in three dimensions, the flow pattern inside the UCG cavity is highly nonideal.⁶ The complexity increases further because of several other physical and chemical processes occurring simultaneously, such as chemical reactions (both homogeneous and heterogeneous), heat transfer due to convection and radiation, mass transport, water intrusion from surrounding aquifers, structural changes in the coal seam due to thermomechanical stresses and other geological aspects.^{7–9}

In the recent past, many research papers on UCG have appeared in the literature, including state-of-the-art reviews on both experimental and modeling work.^{10,11} Because of the complex nature of underground coal gasification, with multiple phenomena at various length and time scales occurring simultaneously, the computational effort involved in computer simulations of UCG process models is considerable. Therefore, in all the existing models in the literature,^{12–24} several assumptions and simplifications have been made in order to ensure tractability, and make predictions of UCG performance. Thus, multi-zonal or phenomenological models, which reduce the complexity without significant compromise on the important features of the process, are critical at this stage for UCG. The overall phenomenological

Received: March 1, 2011

Accepted: December 20, 2011

Revised: December 17, 2011

Published: December 20, 2011

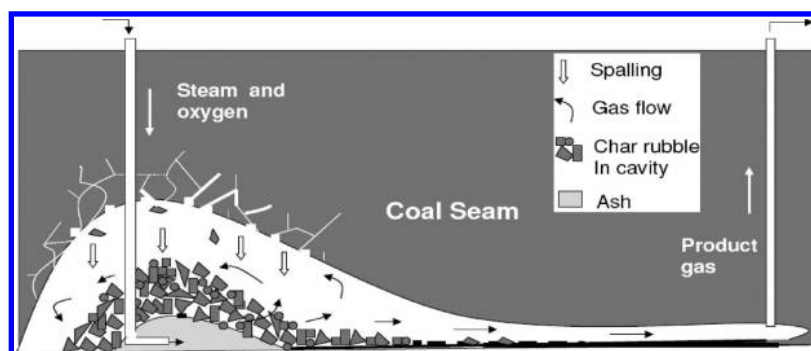


Figure 1. Schematic diagram of the UCG process.

model we envisage for the UCG process is described in our earlier work.⁸ In this paper, the focus is on a few aspects of UCG, and the attempt is to provide a simplified basis that fits well into the framework of an overall process model.

As an important step in the development of a phenomenological model for UCG, we studied the flow patterns in laboratory-scale UCG cavities under isothermal conditions, and the results were presented in our earlier work.⁸ However, in a real situation, significant temperature gradients may exist in the cavity. This is because coal/char in the cavity is available for the reaction at discrete locations in the cavity domain, i.e., either at the roof of the cavity or in the form of spalled particles lying on the floor, or both. The temperature of the coal particles is the net effect of the two main reactions (i.e., exothermic coal/char combustion and endothermic coal/char gasification). Whether or not the coal/char particles are present on the floor of the cavity would be dependent on the spalling tendency of the given coal. Spalling is the detachment of the coal blocks from the roof of the cavity due to thermomechanical stresses developed in the seam. The magnitude of the stress is dependent on the type of coal. Hence, some coals are prone to spalling while some are not. In an extreme situation, if no spalling occurs, then both combustion and gasification will occur at the roof of the cavity. In this case, at any given time, the roof is expected to be at higher temperature than the floor. On the other hand, when significant spalling occurs, combustion takes place mainly on the particles lying on the floor, wherein oxygen gets consumed (traditionally, only just enough oxygen to maintain the temperature is fed in UCG; so the large surface area of coal available on the floor in this limiting case can be assumed to consume the feed oxygen entirely), whereas gasification can take place both on the floor and on the roof. In such a case, the floor temperature is expected to be substantially higher than the roof temperature. In an intermediate situation, when the spalling is not significant, the combustion reaction may occur both on the roof and on the floor of the cavity. The temperature gradients within the cavity may not be significant in such a situation and the cavity is close to being isothermal. The isothermal case has already been analyzed in our earlier work.⁸ In this paper, the focus is on the two nonisothermal scenarios described above.

In nonisothermal situations, the effect of wall-to-wall and wall-to-bulk fluid radiative heat transfer on the flow patterns also must be considered, in addition to convective transport, while simulating the flow field. Overall, the flow pattern is strongly influenced by many operating and structural parameters such as inlet feed flow rate, feed temperature, presence of spalled particles, and the orientation of the inlet nozzle. Computational fluid dynamics

(CFD) is the best tool to visualize, characterize, and quantify the nonideal flow behavior in UCG. Figure 2 shows the three distinct scenarios of thermal boundary conditions considered for the UCG cavity in this study. We propose a modeling strategy for the characterization of flow patterns under different conditions of interest (isothermal and nonisothermal), as shown in Figure 2. The proposed strategy not only gives a clear insight into the flow field of the real UCG cavity but is also likely to reduce the computational burden for complete process simulation.

In our previous work,⁸ a CFD-based compartment modeling (i.e., a network of ideal flow reactors) for the UCG cavity was presented. In the first step, CFD simulations were performed for the isothermal case on five different cavities of chosen size and shape in order to determine flow patterns and corresponding residence time distributions (RTDs). Based on the CFD results and considering RTD as the main criteria, a compartment model was proposed. In the next step, the parameters of the compartment model were estimated so that the RTD of the model is in good agreement with that obtained by CFD simulations under similar conditions. Finally, the developed compartment model was further validated by comparing the reaction-enabled steady-state CFD simulation results with those obtained by solving the compartment model using a steady-state flow sheet simulator (i.e., ASPEN PLUS). The proposed model is generic and was found suitable for all the cavity sizes studied, with model parameters such as residence time, bypass ratio, and so on, varying monotonically with cavity size. The main objective of the earlier work was to propose and validate the compartment modeling approach considering a few specific, isothermal test cases. In the present work, we take a step ahead and consider different possible real scenarios and examine the effect of other operating conditions on the reactant gas flow patterns and hence the compartment model parameters. In particular, the effect of temperature is considered by accounting for the temperature gradients within the cavity reactor. The combustion reaction serves as a source of heat in the cavity. The temperature distribution and, hence, the flow patterns, largely depend on where the combustion occurs inside the cavity. Hence, a relatively high temperature ($\sim 1000\text{ }^{\circ}\text{C}$) was assigned to the bottom wall or the roof of the cavity, depending on whether or not spalling takes place in the cavity.

The article is organized as follows: The importance of convection and radiation on the flow patterns is examined first. Based on the CFD simulation results, different simplified modeling strategies are proposed for the spalling and nonspalling cases. The nonisothermal spalling situation is studied in two parts. First, the entire cavity floor is assumed to be at a sufficiently high

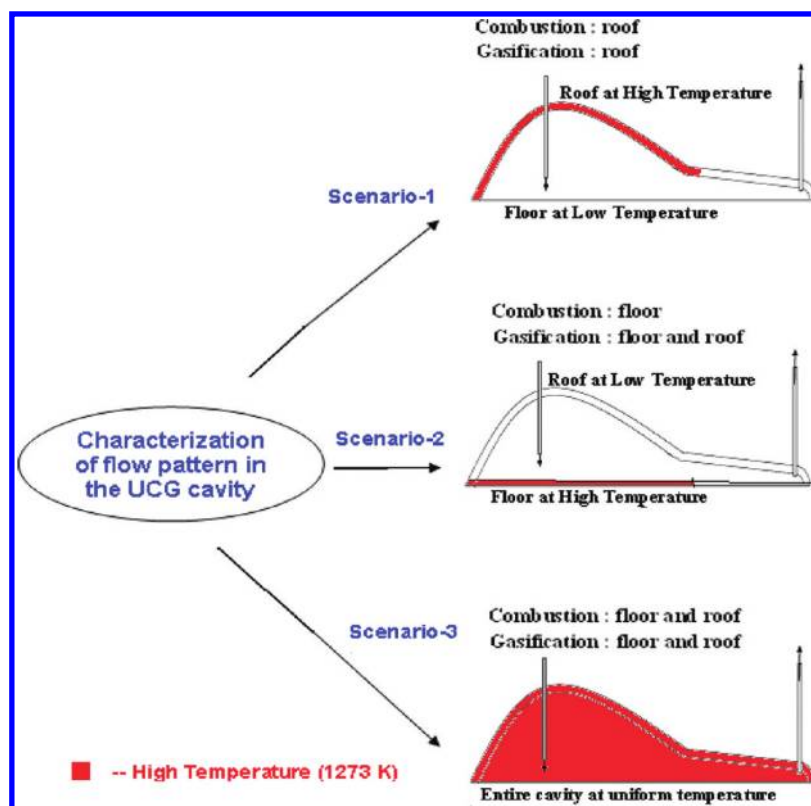


Figure 2. Different possible scenarios of thermal boundary conditions for the UCG cavity.

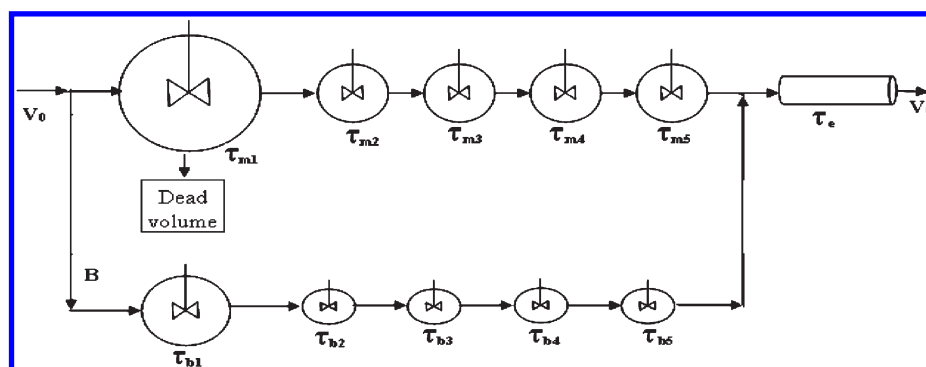


Figure 3. Proposed compartment model.

temperature, compared to the roof, and the effect on the flow patterns is studied. Furthermore, CFD simulations are also performed for nonisothermal conditions at different inlet feed temperatures, feed flow rates, and orientations of the inlet nozzle. The effect of all these parameters on the reactant gas flow patterns in the UCG cavity is quantified with the help of the validated compartment model, and the trends are explained.

2. METHODOLOGY

The methodology used to characterize the flow patterns under different specified conditions is similar to the one described in our earlier work⁸ and is mentioned below briefly.

- CFD simulations are performed on the three cavities studied earlier, in order to determine the steady-state flow patterns of the reactant gases under appropriate boundary and

physical conditions, such as inlet temperatures, flow rates, spalling and nonspalling cases, and orientations of the inlet nozzle.

- In the second step, the steady-state flow field obtained in the first step is frozen and a tracer is introduced as a pulse at the inlet and the unsteady-state model for the tracer balance is solved in order to obtain the RTD.
- Using the RTD, parameters for the validated compartment model (see Figure 3) are determined using the optimization tool in Matlab, over a range of operating conditions.

3. CFD SIMULATIONS

Geometry. In order to study the flow patterns under different situations, cavity sizes 1, 2, and 3 for a vertical injection of reactants studied earlier⁸ are chosen here as well. The sizes of the

Table 1. Boundary Conditions and Other Specifications Used for CFD Studies

feed temperatures	1073 K, 873 K, 673 K
feed velocities	4 m/s, 6 m/s, 8 m/s
inlet velocity	4 m/s
feed temperature	673
carrier fluid	oxygen
outlet pressure	5 atm
viscous model	realizable $k-\varepsilon$

cavities were chosen based on the relevant information available in the literature.^{6,18} The dimensions of the cavities and the grid used for the simulations can be found elsewhere.⁸ The geometry is created for the cavity and converted into discrete control volumes (i.e., meshed) using the commercial CFD meshing preprocessor, GAMBIT. The optimized grid size is determined after grid independency tests which are detailed in our earlier work.⁸ The type and size of the mesh selected for the CFD simulations and the criterion for the grid independency test are also as described in our earlier work.⁸ A separate geometry was created for the spalling case by considering the spalled particles (equally sized spherical particles 5 cm in diameter at a uniform distance of 5 cm) uniformly laid out on the floor of the cavity.

Input Specifications and Convergence Criteria. At the inlet, a “velocity_inlet” boundary condition is used and three different velocities (4, 8, and 16 m/s) are specified, such that the incoming feed has volumetric flow rates of 113.14, 226.28, and 452.56 m³/h, respectively. A “pressure outlet” boundary condition was used at the outlet with the gauge pressure of 5 atm, which is assumed based on the field trial data.²⁵ For the nonspalling case, the presence of reaction at the roof was indirectly considered by imposing a high-temperature (a constant wall temperature, 1273 K) boundary condition at the roof, whereas the rest of the cavity walls, which are expected to be composed of rock or mud, were assumed to be losing heat to the surroundings at a constant heat flux of 25 W/(m² K). The magnitude of this heat flux is based on the information available in the literature.²⁶ In case of spalling, the cavity bottom, where the combustion is expected to occur, is considered to be present at a constant wall temperature (i.e., 1273 K) and the other walls are assumed to be losing heat at a constant flux of 25 W/(m² K). The realizable $k-\varepsilon$ model with standard wall functions is used in these computations in order to model turbulent flow in the cavity. This scheme is suitable for flow involving recirculations.^{27,28} The boundary conditions used for this study are given in Table 1.

In order to study the effect of radiation on the flow patterns, the P-1 radiation model²⁸ is considered while simulating the flow field. The P-1 model works well for combustion applications where the optical thickness is large.²⁸ The model can be easily applied to complicated geometries, such as UCG cavities, with curvilinear coordinates. It is easy to solve the model equations with little CPU demand and with reasonable accuracy.^{28,29} Based on the work of Kuyper et al.,³⁰ and Perkins and Sahajwala,³¹ the extinction coefficient for the gas is assumed to be constant 0.12 m⁻¹ (absorption coefficient = 0.12 m⁻¹ and it is also assumed that it scatters in all directions equally). Simulations using other radiation models (including the gray gas model or the discrete ordinate model) for the absorption coefficient did not show any significant difference. The equations for the conservation of mass, momentum, energy, and radiation (see eqs 1, 2, 3 and 4)

in the turbulent regime for these meshed geometries are solved in order to obtain the steady-state flow patterns under the specified boundary conditions using the CFD software, FLUENT v6.3.26.

Continuity Equation:

$$\frac{\partial \rho}{\partial t} + \nabla \cdot (\rho \vec{v}) = 0 \quad (1)$$

Momentum Equation

$$\frac{\partial}{\partial t}(\rho \vec{v}) + \nabla \cdot (\rho \vec{v} \vec{v}) = -\nabla p + \nabla \cdot (\bar{\tau}) + \rho \vec{g} + \vec{F} \quad (2)$$

Energy Balance Equation

$$\frac{\partial}{\partial t}(\rho E) + \nabla \cdot (\vec{v}(\rho E + p)) = -\nabla \cdot \left(\sum_j h_j \vec{J}_j \right) \quad (3)$$

P-1 Radiation Model

$$-\nabla \cdot q_r = aG - 4a\sigma T^4 \quad (4)$$

The SIMPLE (Semi-Implicit Method for Pressure-Linked Equations) algorithm is used to resolve the pressure–velocity coupling and a steady-state second-order upwind discretization model is used to solve the above equations. In the case of steady-state simulations, the solution is judged to be converged when the scalar residuals of each transport equation goes below 1×10^{-7} . The mass flow difference between “in” and “out” is checked and is of the order of 10^{-8} . For each cavity size, three independent simulations are performed in order to study the effect of feed temperature, and another three independent simulations for the effect of feed flow rate. Furthermore, several simulations are performed in order to examine the effect of orientation of the inlet nozzle and spalling.

RTD Simulations. Once a steady-state solution is obtained for the cavity under the specified conditions, the flow field is frozen. In order to perform the virtual tracer experiments, a tracer, which has similar properties as the carrier fluid, is injected into the cavity as a pulse (i.e., at time = 1 s, the feed consists of a tracer mass fraction of 1.0). In order to minimize diffusion effects, the diffusivity of the tracer is taken as a sufficiently low value (i.e., 1×10^{-15} m²/s). The unsteady-state model is solved for the governing species balance (eq 5) in order to obtain the concentration profile of the tracer. In the unsteady-state simulations, temporal accuracy for species balance equation is solved until the scalar residue of this equation reduces to $<1 \times 10^{-7}$. The RTD is calculated from the area-weighted average of tracer concentration data against time, obtained at the outlet. Exit age distribution (*E*-curve) data are generated for all of the cavity sizes. For each cavity size, *E* curve data are generated at three feed temperatures, three flow rates, two inlet nozzle orientations, and in the presence/absence of spalling.

Species Balance Equation:

$$\frac{\partial}{\partial t}(\rho Y_i) + \nabla \cdot (\rho \vec{v} Y_i) = -\nabla \cdot \vec{J}_i \quad (5)$$

4. COMPARTMENT MODELING

Compartment modeling is a technique used to characterize reactors of irregular geometries and complex flow patterns.

Table 2. Compartment Model Parameters for Effect of Feed Temperature

model parameter	Cavity Size 3			Cavity Size 2			Cavity Size 1		
	1073 K	873 K	673 K	1073 K	873 K	673 K	1073 K	873 K	673 K
V_{M1} (m ³)	39.252	36.104	29.151	12.168	12.00	10.288	2.351	2.284	2.035
V_{M2} to V_{M5} (m ³)	0.400	0.352	0.246	0.333	0.320	0.226	0.251	0.223	0.217
V_{B1} (m ³)	2.000	1.020	0.129	0.960	0.300	0.100	0.079	0.077	0.007
V_{B2} to V_{B5} (m ³)	0.095	0.062	0.014	0.054	0.050	0.012	0.041	0.035	0.007
V_P (m ³)	0.700	0.330	0.270	0.500	0.300	0.230	0.360	0.290	0.200
bypass ratio, B	0.099	0.092	0.004	0.120	0.110	0.026	0.153	0.143	0.047
total active volume (m ³)	43.932	39.110	30.590	15.175	14.08	11.569	3.960	3.685	3.138
% dead volume	5.443	15.822	34.159	4.281	11.19	27.023	3.334	10.047	23.400
% error	1.503	0.984	1.557	1.533	2.146	1.270	2.210	0.97	1.977

Such geometries are viewed as ideal reactor networks that also include bypass, recycle streams, and dead volumes. In our earlier work, a compartment model (see Figure 3) was proposed for the UCG cavity based on velocity vectors, path lines, and E -curves obtained from CFD simulations. The basic structure of the compartment model remains the same for the current study and only the model parameters (residence times of the individual reactors and the bypass ratio) differ under different thermal conditions.

Formulation of the Compartment Model. In formulating the compartment model, unsteady-state tracer balance equations for each reactor may be written as

Main stream reactors:

$$\frac{dC_{m,i}}{dt} = \frac{C_{m,i-1} - C_{m,i}}{\tau_{m,i}} \quad (6)$$

This equation represents the species mass balance for all of the continuously stirred tank reactors (CSTRs) in the main stream of the compartment model shown in Figure 3.

Parallel stream reactors:

$$\frac{dCb_k}{dt} = \frac{Cb_{k-1} - Cb_k}{\tau_{bk}} \quad (7)$$

In Figure 3, the bypass stream is seen to consist of five other CSTRs. Equation 7 represents the species mass balance for these reactors:

For time = 1 s:

$$C_{m,1} = C_{b,1} = 1 \quad (8)$$

For time > 1 s:

$$C_{m,i} = C_{b,i} = 0 \quad (9)$$

for $j = 1-5$ (the number of reactors in series).

These boundary conditions (eqs 8 and 9) represent the pulse injection of the tracer, at time = 1 s, as discussed earlier. The set of unsteady-state differential equations (eqs 6 and 7) are solved using the ode15s solver in MATLAB in order to obtain the exit concentrations of CSTRs in both the main and the bypass streams. The delay time (i.e., the residence time of the plug-flow reactor (τ_P) in Figure 3) for the tracer concentration at the outlet is obtained from

the E -curve. Finally,

For $i = 1$ to τ_P :

$$C_{out} = 0 \quad (10)$$

For $i = \tau_P$ to the total operation time:

$$C_{out} = (1 - b)C_{m5} + (b \times C_{b5}) \quad (11)$$

where b is the ratio in which the inlet stream splits as indicated in Figure 3.

Equations 10 and 11 provide the outlet tracer concentration predicted by the compartment model at any point in time. This is used to evaluate the RTD, $E(t)$, using the standard formula for pulse tracer inputs.

The E -curves of the compartment model are fitted to the one obtained from the CFD simulations using the NLINFIT optimization tool in MATLAB, in order to estimate the model parameters (reactor residence times). The optimizer used to determine the parameters requires two inputs (i.e., initial guesses for all the parameters to be estimated, and the target E -curve data (in our case, this is the CFD data) over a certain time period). The parameters thus obtained for all the cases are given in Tables 2–5. The goodness of the fit was measured in terms of the average percentage error (e), which was <3% in all cases.

The CFD simulations required for compartment modeling described above can be simplified further under certain operating conditions, as explained in the following sections.

5. RESULTS AND DISCUSSIONS

There are two important modes of heat transfer in the UCG cavity, viz convection (due to the flow of gas in the cavity) and radiation (due to the high wall temperatures). The temperature field at steady state is a result of the net effect of these two phenomena, and the reactant fluid flow pattern is also strongly linked with it. In the following section, we study the interplay of convection and radiation in the cavity for both the spalling and nonspalling cases, and also explore the possibility of simplifying the compartment modeling approach under specific conditions. For the sake of consistency, all the results reported below are for the cavity size 1. Our simulations and analysis indicate that the observed trends are general and applicable to each of the three cavity sizes studied here.

Scenario I: Nonspalling—Combustion at the Roof. In order to study the effect of heat transfer due to radiation, CFD

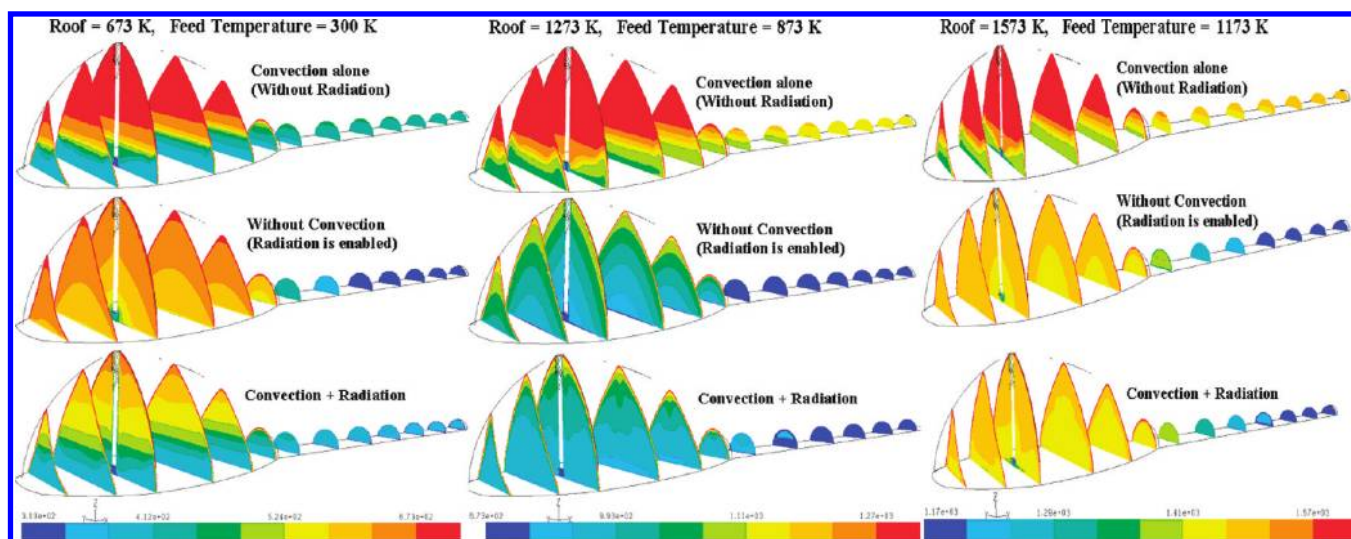


Figure 4. Comparison of temperature contours for the cases of convection alone, radiation alone, and convection along with radiation (nonspalling case). (Temperatures are given in Kelvin.)

simulations are performed with the help of a commonly used P-1 radiation model. In the first step, the simulations are performed for a chosen cavity size 1 in the absence of spalling, i.e., when the cavity roof is at a higher temperature than the floor. To examine the importance of convection over the other modes of heat transfer, we compare the convection-enabled simulation results with the convection-disabled CFD simulation results. Figure 4 shows the comparison of three different cases. In case 1, we have performed simulations by considering convection alone, i.e., without enabling radiation. Case 2 shows the results when the convection is not considered and only radiation is enabled, i.e., the momentum equation is disabled, while case 3 shows results generated by considering both radiation and convection. Results for each case are obtained at three different roof temperatures. It should be noted here that case 1 and case 2 are purely hypothetical situations of course, and the simulations are done under these conditions only to examine the relative importance of convection. Comparison of case 3 with case 1 and case 2 tells us which mode of transfer prevails in the cavity at high temperatures. From Figure 4, it is observed that, at lower roof temperatures, both modes of heat transfer (i.e., convection and radiation) are prevalent, whereas, at higher temperatures, convection is not important when compared with radiation.

The flow patterns are well-characterized by exit age distribution, and we perform virtual tracer studies, the procedure of which is outlined in section 2. Figure 5 shows a comparison of the RTD for two cases: convection alone and convection + radiation for a high roof temperature (1273 K) case. The peak height of the E -curve reduces significantly in the presence of radiation, which suggests a larger active volume, whereas the sharp initial peak for the case of convection alone indicates that a significant portion of the feed stream bypasses the main cavity. Figure 6 shows the flow field (velocity contours and path lines) for the two cases mentioned above (for a high roof temperature (1273 K) case). It can be seen that radiation is responsible for relatively intense mixing, giving rise to a larger active volume.

Thus, the temperature distribution in the cavity is mainly governed by radiation in the absence of spalling, at high roof temperatures. This allows us to decouple the energy and momentum

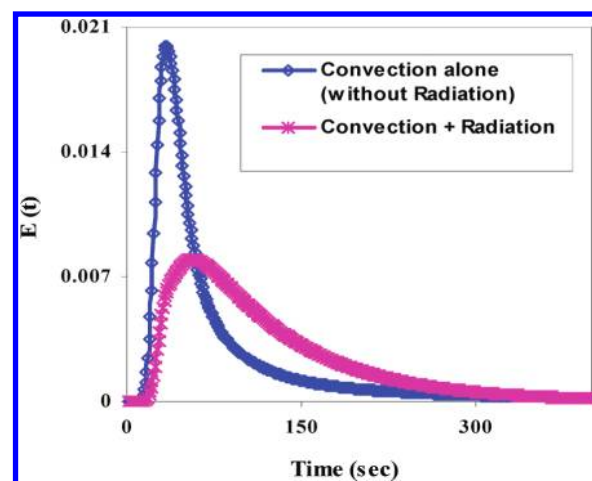


Figure 5. Comparison of E -curves of both radiation and nonradiation (nonspalling case, roof temperature = 1273 K, and feed temperature = 873 K).

balance equations in CFD simulations; hence, a simplified methodology can be adopted for the nonspalling case, as given in Figure 7. First, CFD simulations are performed in order to obtain the temperature field alone for a chosen cavity size by solving the energy balance, incorporating only radiation as a means of heat transfer. Once the steady state is obtained, the temperature field is frozen and the mass and momentum balance equations are solved using the fixed temperature field, and a steady-state flow field is obtained. In the next step, unsteady-state tracer simulations are performed to obtain the RTD (E -curve) after freezing the steady-state flow field. To validate this approach, steady-state CFD simulations are performed under similar conditions to solve the mass, momentum, energy, and radiation equations simultaneously and virtual tracer studies are also performed to get the E -curve after freezing the steady-state flow and energy field. Figure 8 shows that the two E -curves—one obtained with an expensive CFD simulation involving simultaneous solution of the mass, momentum, and energy balances, and the other with our simplification for the specific situation of

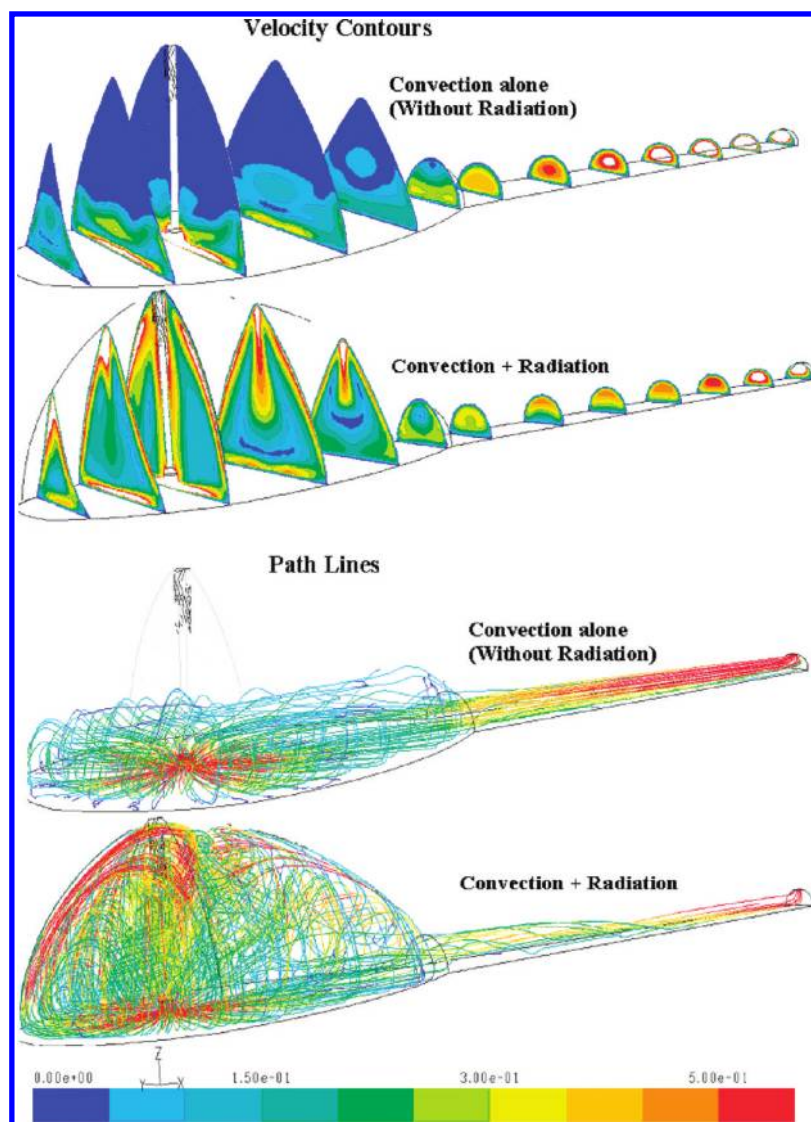


Figure 6. Comparison of velocity magnitudes and path lines of both convection alone and convection along with radiation (nonspalling case, roof temperature = 1273 K, and feed temperature = 873 K).

high feed and roof temperatures—are in good agreement with each other. Based on the results of Figure 4 and the discussions above, we can conclude that the proposed methodology is applicable only when both cavity roof and feed temperatures are at sufficiently high values.

Scenario II: Spalling—Combustion on the Cavity Floor.

A similar procedure is used to study the influence of convection on the flow patterns when spalling occurs. In this case, cavity floor is assigned a temperature of 1273 K and rest of the walls are assumed to dissipate energy to the surrounding at a constant heat flux of $25 \text{ W}/(\text{m}^2 \text{ K})$.²⁶ CFD simulations are again performed for case 1 (convection alone), case 2 (convection disabled), and case 3 (convection along with radiation). Figure 9 shows a comparison of the temperature contours for the three cases, for two different feed temperatures, and it is observed that, for the higher cavity temperatures (roof = 1273 K and feed = 873 K), case 1 and case 3 are close to each other. In the same figure, we can also see the temperature contours for the case when the roof temperature is 1273 K and the feed temperature is 300 K. We can conclude that, unlike in Figure 4 above, convection plays an important

role at all feed temperatures. Thus, convection dominates over radiation in this case. This is because of the intense buoyancy-driven circulation caused by the large temperature difference between the floor of the cavity and the roof wall. The feed gas is released from the inlet, which is close to the cavity floor, and is suddenly exposed to the high-temperature region, leading to a decrease in density and a flux in the upward direction where it encounters the relatively cold roof. This induces buoyancy-driven flow, which leads to rigorous back mixing in the cavity.

Independent virtual tracer experiments are performed at various feed temperatures to verify the effect of radiation in the case of spalling. Based on these results, a simplified modeling strategy is proposed for the characterization of flow patterns in the case of spalling, which is shown in Figure 7. In this case, CFD simulations are performed to solve the mass, momentum, radiation, and energy balance equations simultaneously. Virtual tracer experiments are performed to obtain the *E*-curve. A similar exercise is performed by disabling the radiation to get the *E*-curve. The time required to get the *E*-curve for the case of radiation-enabled situation is much more than that with the radiation-disabled case,

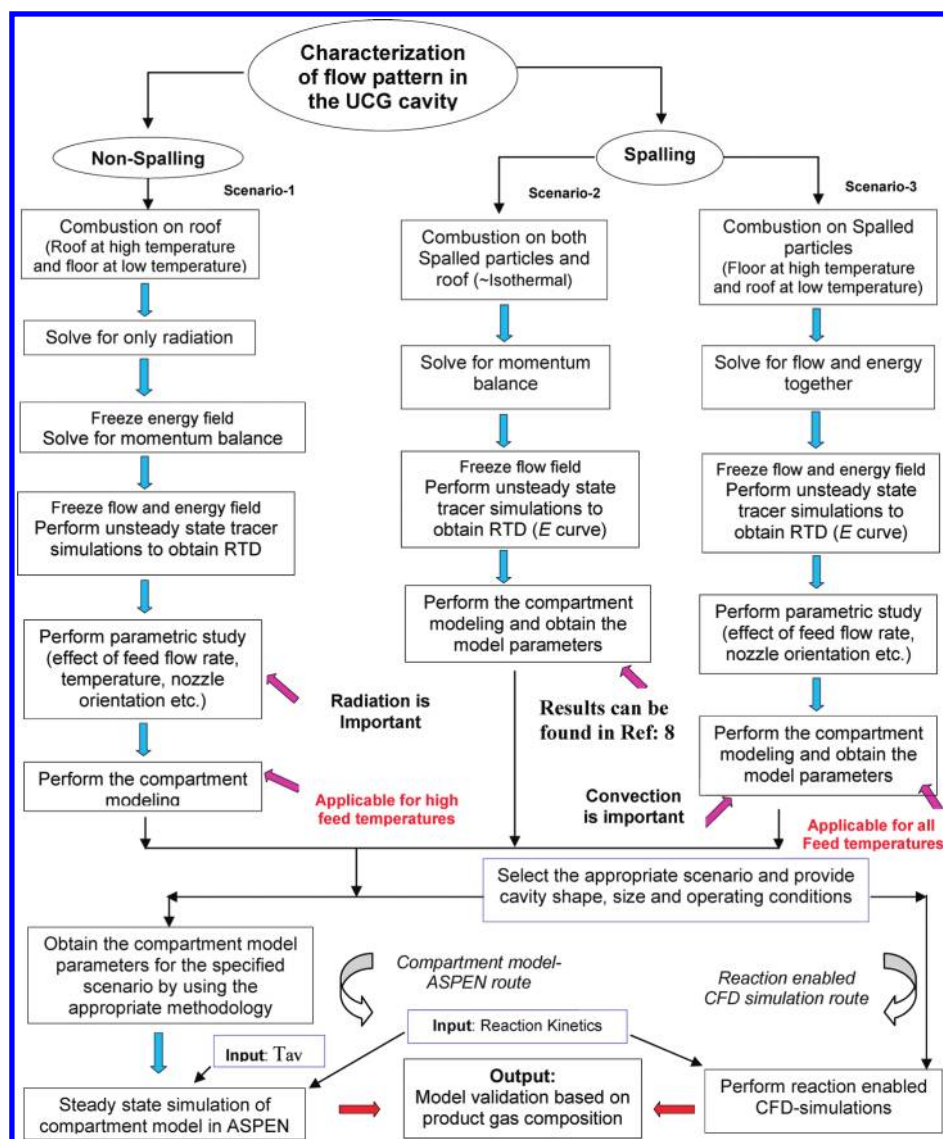


Figure 7. Block diagram for the methodology of characterization of flow pattern.

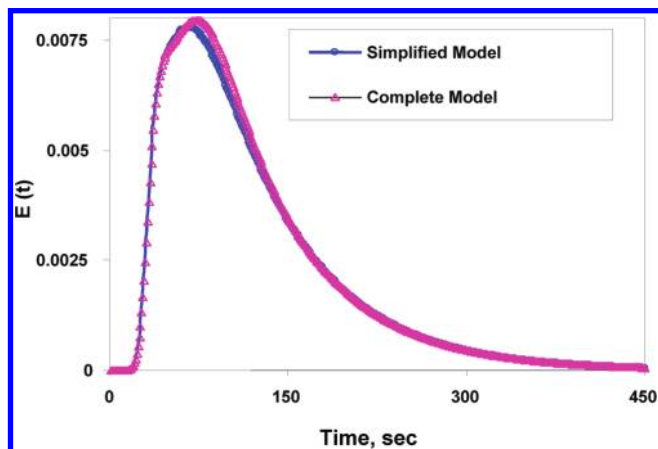


Figure 8. Comparison of E -curves obtained from both complete model and simplified methods (nonspalling case).

because solving all the transport equations together is computationally expensive. The E -curves obtained from both the radiation-enabled

and radiation-disabled cases are compared in Figure 10, which shows that the E -curves for both these cases are similar. Thus, for the spalling case, radiation can be safely neglected, with considerable savings in computational expense (120 CPU hours).

Effect of Feed Temperature. The inlet feed temperature has a significant impact on the efficiency of gasification in the UCG process. Three different feed temperatures (i.e., 673, 873, and 1073 K) are chosen here in order to study the cavity flow pattern in a nonspalling case. By keeping other boundary conditions similar, three independent simulations are performed to obtain the steady-state flow patterns and the E -curve for all the cavity sizes. In order to quantify this effect, the parameters of the compartment model are also estimated. Figure 11a shows the path lines (colored by velocity magnitude, m/s) of the injected tracer in a chosen cavity size 1 at a particular time, which clearly shows that, at low temperatures, the active volume is lower. This is due to the fact that, at higher feed temperature, the overall cavity temperature increases (see Figure 12a), which results in a higher volumetric flow rate and, hence, more mixing in the cavity.

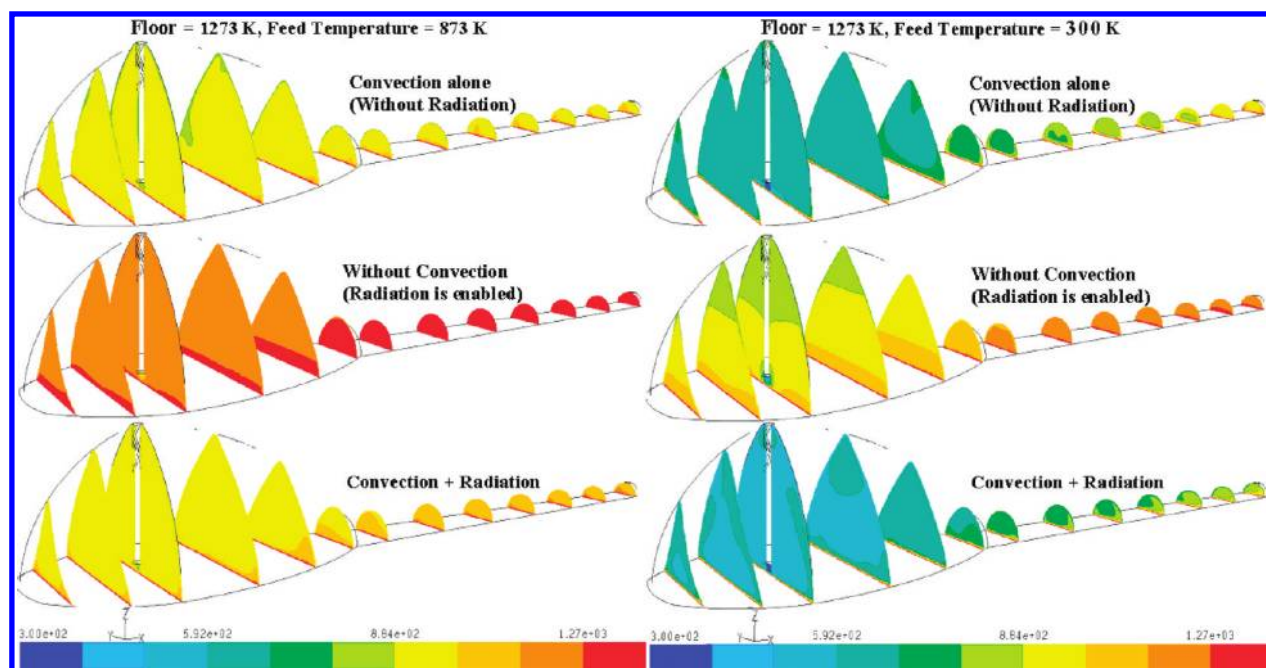


Figure 9. Comparison of temperature contours for the cases of convection alone, radiation alone, and convection along with radiation (spalling case). (Temperatures are given in Kelvin.)

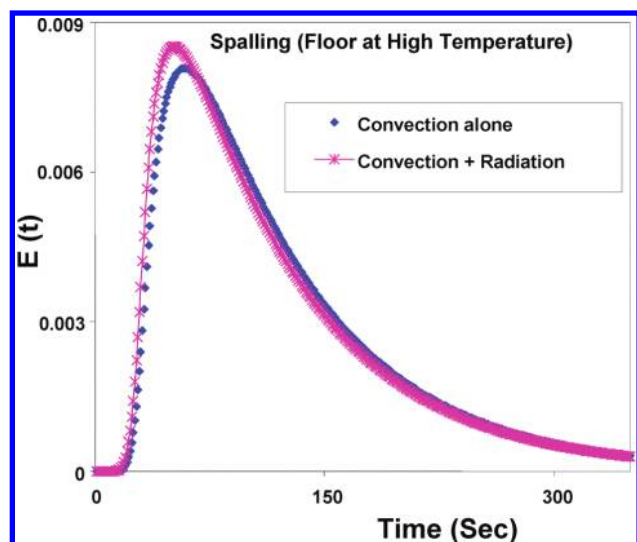


Figure 10. Comparison of E -curves obtained from both convection alone and convection along with radiation (spalling case).

The E -curves at various feed temperatures for a chosen cavity size 1 are shown in Figure 13a. By increasing the feed temperature, the magnitude of the peak in the E -curve decreases, which indicates that there is an increment in the active volume. The compartment model parameters are given in Table 2. It can be seen that the volumes of all the back-mixed reactors in the main stream, as well as in the parallel stream, and the plug-flow reactor increase with feed temperature, which leads to a corresponding reduction in the dead volume. It also shows that the bypass ratio increases as the feed temperature increases. The trends in model parameters (reported in Table 2) are consistent with the observations made from the E -curve.

Effect of Flow Rate. Three different flow rates (i.e., 4, 8, and 16 m/s) are chosen to study the effect of flow rate on the

flow pattern. These simulations are performed for the nonspalling case with a feed temperature of 873 K. Figure 11b shows the path lines (colored by velocity magnitude, m/s) of the injected pulse for three different flow rates and for a chosen cavity size 1. It is observed that, at low flow rates, feed gas is not well-distributed within the cavity. As expected, for a given cavity size, internal mixing increases with an increase in feed flow rate, which can be seen in Figure 11b. By increasing the feed flow rate, forced convection dominates over buoyancy-driven convection, because the temperature in the cavity is uniform and relatively low (see Figure 12b). This is also confirmed from the velocity vector plots, which are not shown here.

Table 3 depicts the compartment model parameters for the effect of feed flow rate in all the cavities. It can be seen that the volumes of all the reactors of the compartment model increase as the flow rate increases at a given cavity size. This is due to enhanced internal circulation and increase in the overall active volume. A corresponding decrease in the percentage of dead volume can be seen in Table 3. As expected, for a fixed flow rate, the dead volume increases as the cavity size increases under otherwise similar conditions, as also observed in our earlier work on isothermal cavities.⁸ Furthermore, the bypass ratio decreases with an increase in the cavity size. The predicted model parameters are consistent with the trends observed from the plots of path lines and RTD. Figure 13b shows the comparison of RTDs of different feed flow rates for a chosen cavity size 1. The trend in positions and heights of the peaks in the E -curve with changes in the flow rate is consistent with the explanation given above.

Effect of Nozzle Orientation. Two different injections (i.e., vertical and horizontal) are considered in order to study the effect of inlet nozzle orientation on the flow patterns. The simulations are performed under similar operating conditions (i.e., feed flow rate = 4 m/s and feed temperature = 873 K) in the nonspalling case. Figure 11c shows the comparison of path lines (colored by velocity magnitude, m/s) for both injections. It indicates that,

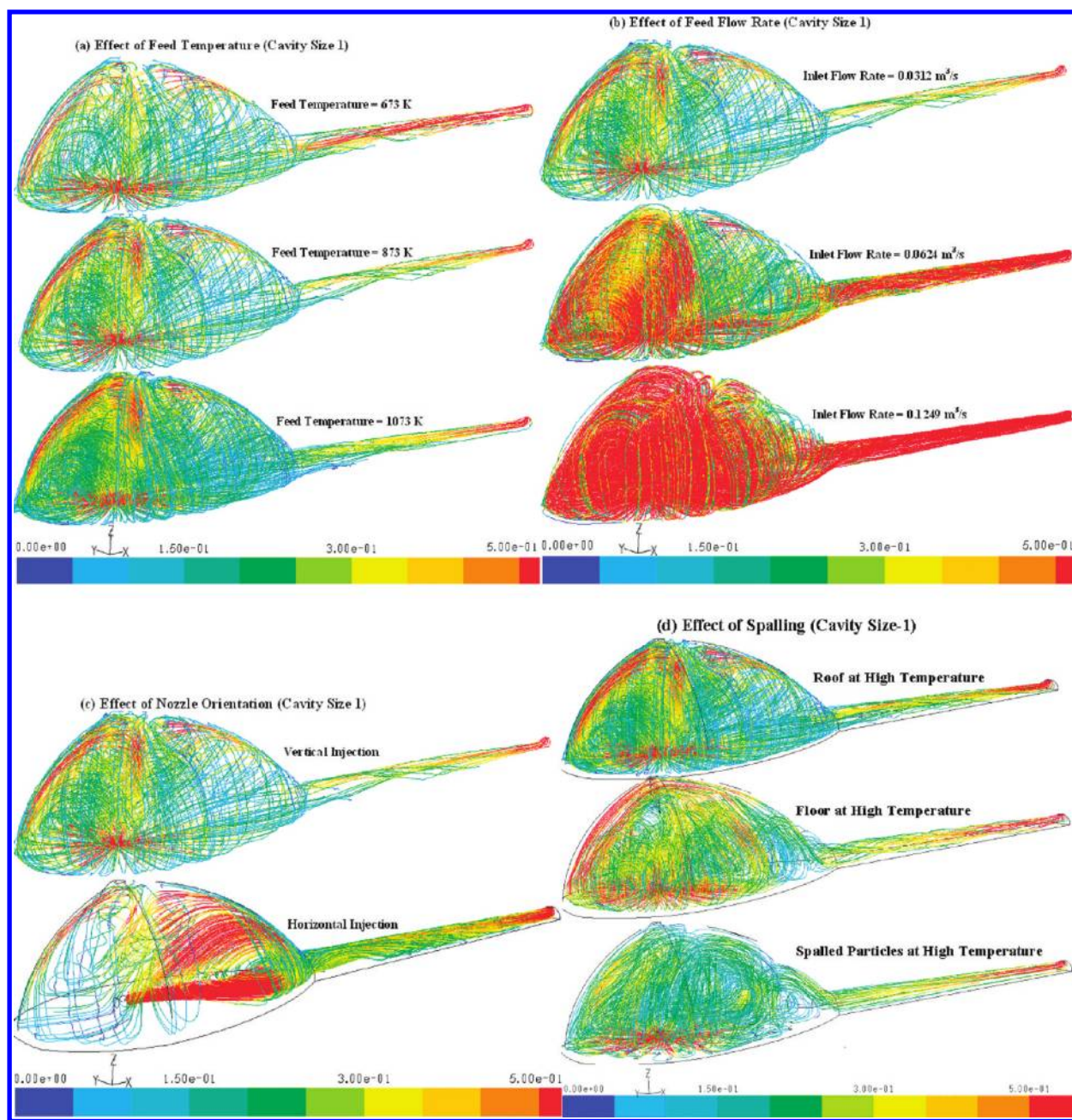


Figure 11. Comparison of path lines (colored by velocity magnitude, m/s) for all cavity sizes with specific conditions.

for vertical injection, flow distribution occurs throughout the cavity, which leads to a decrease in the temperature gradient (see Figure 12c) whereas, in case of horizontal injection, by virtue of its orientation, maximum mixing occurs only in the forward region of cavity. The dead volume is more in the case of horizontal injection, as a substantial part of the feed stream bypasses the cavity. Figure 13c gives the comparison of the RTDs for both vertical and horizontal injections for a chosen cavity size 1. It can be seen that the magnitude of the peak in the E -curve is less for the vertical injection, which is an indication of larger active volume. The E -curve, in the case of horizontal injection indicates higher bypass, less initial time delay, and larger dead volume. In order to quantify the above-mentioned observations, compartment modeling is performed independently for both

vertical and horizontal injections with the help of respective E -curves.

The compartment model parameters are given in Table 4. As expected, the volumes of the mixed reactors in the main stream, as well as the plug-flow reactor, are more for vertical injection, and they increase with cavity size. Furthermore, it can be seen that the volumes of mixed reactors in the side stream are more for horizontal injection, compared to vertical injection, as a large fraction of the feed stream bypasses the cavity. Hence, vertical injection favors better utilization of the cavity volume than horizontal injection. As the cavity size increases, the bypass ratio decreases.

Effect of Spalling. Three independent CFD simulations were performed to study the effect of spalling in the cavity. The effect

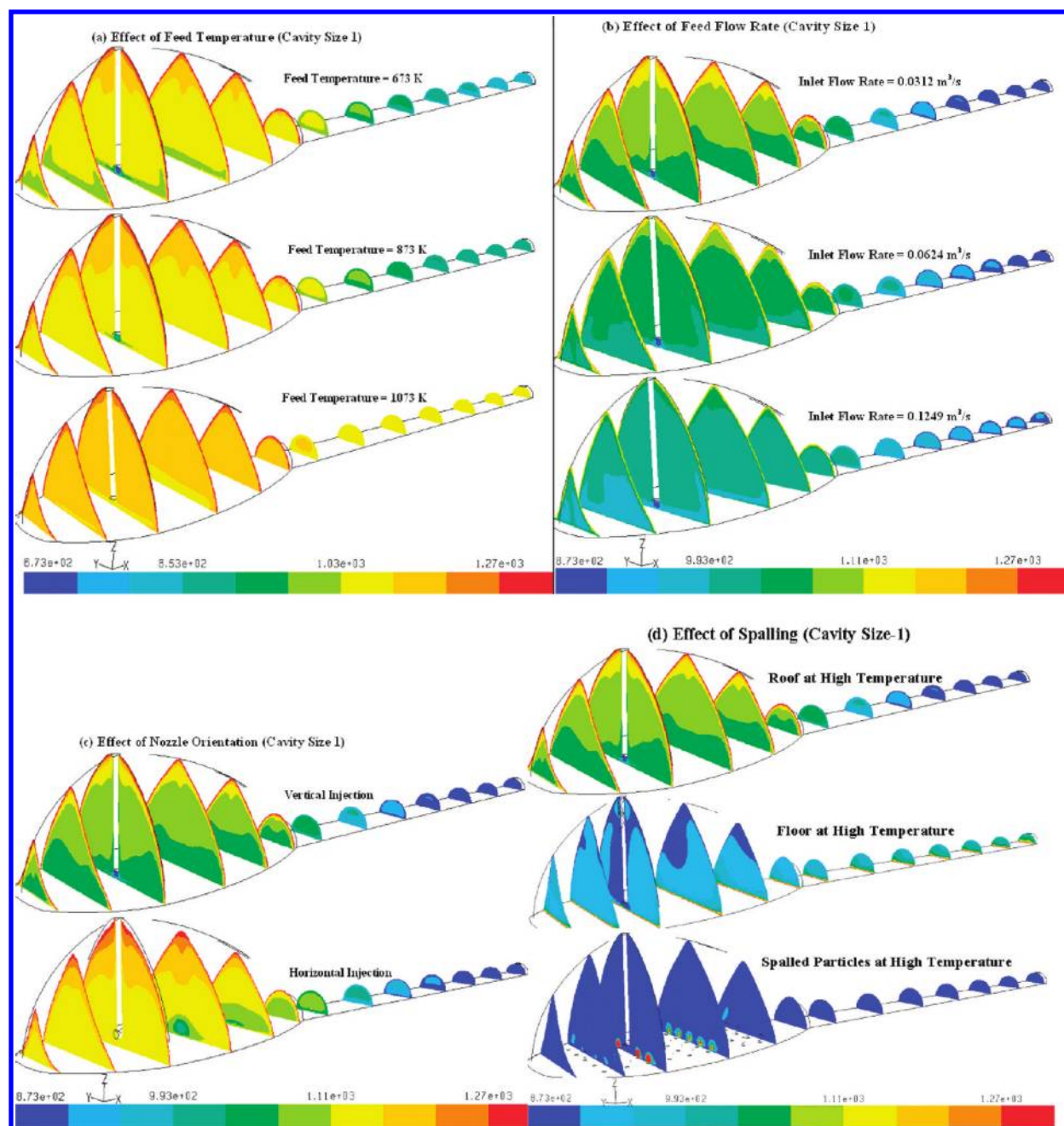


Figure 12. Comparison of temperature contours for all cavity sizes with specific conditions. (Temperature are given in Kelvin.)

is studied in two steps. In the first step, the cavity floor is assumed to be at a higher temperature than the roof. In this case, the flow pattern is driven by the temperature gradient. In the second step, the presence of spalled particles (at high temperature) is considered at the cavity bottom, causing obstruction to the flow to facilitate back mixing. In the latter case, the flow pattern is affected by both the spalled particles and the temperature gradients. In order to compare these results with the nonspalling case, CFD simulations are also performed by assuming the cavity roof at a high temperature (nonspalling case). All these simulations are performed under otherwise similar operating conditions, such as feed flow rate, feed temperature, and pressure. Figure 12d shows a comparison of temperature contours

(in Kelvin) on different vertical planes, along with the axial direction for a chosen cavity size 1. It indicates that the temperature is relatively uniform in the cavity for the spalling case, compared to the nonspalling case. In case of spalling, the feed gas immediately gets exposed to a high temperature zone near the inlet and tends to move toward the low temperature region near the roof. This leads to an increase in internal circulations, which are responsible for the higher active volume in the case of spalling.

Figure 11d shows the comparison of path lines (colored by velocity magnitude, m/s) for both spalling and nonspalling cases of a selected cavity size 1 for the chosen time steps. It indicates that internal circulations occur, in the case of spalling.

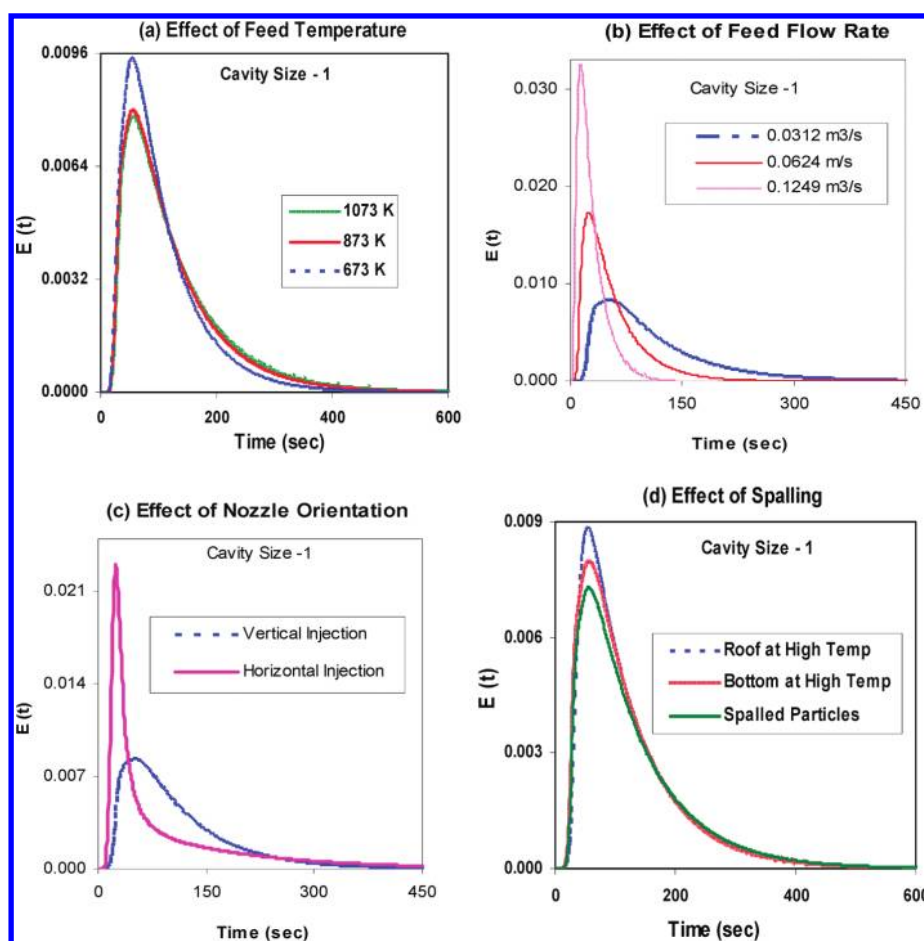


Figure 13. Comparison of RTD for all cavity sizes with a specific conditions.

Table 3. Compartment Model Parameters for Effect of Feed Flow Rate

model parameter	Cavity Size 3			Cavity Size 2			Cavity Size 1		
	16 m/s	8 m/s	4 m/s	16 m/s	8 m/s	4 m/s	16 m/s	8 m/s	4 m/s
V_{M1} (m ³)	39.500	38.459	36.104	12.520	12.485	12.000	2.315	2.280	2.284
V_{M2} to V_{M5} (m ³)	0.511	0.380	0.352	0.406	0.334	0.320	0.280	0.260	0.223
V_{B1} (m ³)	1.812	1.469	1.020	0.758	0.609	0.300	0.097	0.092	0.077
V_{B2} to V_{B5} (m ³)	0.153	0.118	0.062	0.109	0.075	0.050	0.060	0.059	0.035
V_P (m ³)	0.400	0.360	0.330	0.360	0.320	0.300	0.320	0.300	0.290
bypass ratio, B	0.141	0.125	0.092	0.194	0.150	0.110	0.298	0.272	0.143
total active volume (m ³)	44.369	42.281	39.110	15.700	15.048	14.080	4.093	3.947	3.685
% dead volume	4.503	8.997	15.822	0.971	5.085	11.188	0.065	3.639	10.047
% error	0.565	2.130	0.984	2.535	2.986	2.146	1.799	1.38	0.97

Particularly in the case of spalling 2, i.e., in the presence of spalled particles, more mixing occurs due to the obstruction to flow by the spalled particles present on the floor of the cavity. It also indicates that the active volume is more in the case of spalling. The comparison of RTDs of spalling case and nonspalling cases of a selected cavity size 1 is shown in Figure 13d.

The initial sharp peak is observed in the case of nonspalling case indicating that the fraction of the feed stream that is bypassing the cavity immediately (bypass ratio is more). The magnitude of the peak in the E -curve is less for the spalling case,

which suggests that the active volume is relatively larger. Table 5 gives the compartment model parameters, which indicate that the volumes of mixed reactors in the main stream and that of the plug-flow reactor are more for the spalling case, compared to that of the nonspalling case. As expected, the parameters are significantly different from those in the isothermal case.⁶ For example, in the case of isothermal cavities (1000 °C), the dead volumes are <1% for all the cavity sizes, whereas, for the nonisothermal case, it varies in the range of 10%–15% under otherwise identical conditions. This is because of the lower

Table 4. Compartment Model Parameters for Effect of Nozzle Orientation

model parameter	Cavity Size 3		Cavity Size 2		Cavity Size 1	
	VI	HI	VI	HI	VI	HI
V_{M1} (m ³)	36.104	34.144	12.0	11.539	2.284	1.771
V_{M2} to V_{M5} (m ³)	0.352	0.162	0.320	0.168	0.223	0.0904
V_{B1} (m ³)	1.020	0.022	0.300	0.050	0.077	0.3373
V_{B2} to V_{B5} (m ³)	0.062	0.008	0.050	0.034	0.035	0.0272
V_P (m ³)	0.330	0.200	0.300	0.220	0.290	0.27
bypass ratio, B	0.092	0.088	0.110	0.206	0.143	0.232
total active volume (m ³)	39.110	35.046	14.080	12.616	3.685	2.849
% dead volume	15.822	24.570	11.188	20.424	10.047	30.44
% error	0.984	2.319	2.146	1.517	0.97	1.25

Table 5. Compartment Model Parameters for the Effect of Spalling

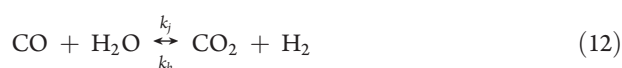
model parameter	Cavity Size 3		Cavity Size 2		Cavity Size 1		
	BHT	RHT	BHT	RHT	BHT	RHT	SP-BHT
V_{M1} (m ³)	41.047	36.104	12.682	12.000	2.338	2.284	1.417
V_{M2} to V_{M5} (m ³)	0.389	0.352	0.371	0.320	0.277	0.223	0.101
V_{B1} (m ³)	0.184	1.020	0.160	0.300	0.058	0.077	1.293
V_{B2} to V_{B5} (m ³)	0.058	0.062	0.047	0.050	0.020	0.035	0.136
V_P (m ³)	0.450	0.330	0.435	0.300	0.420	0.290	0.385
bypass ratio, B	0.098	0.092	0.243	0.110	0.277	0.143	0.368
total active volume (m ³)	43.468	39.110	14.949	14.080	4.003	3.685	4.044
% dead volume	6.442	15.822	5.708	11.188	2.279	10.047	1.274
% error	0.841	0.984	1.512	2.146	0.650	2.628	1.108

average temperature and, hence, the lower volumetric flow rates in the latter case. This shows the importance of enabling the energy balance and considering the nonisothermal conditions.

6. VALIDATION OF THE COMPARTMENT MODEL

In our previous work,⁸ the developed compartment model was validated by comparing the homogeneous water-gas shift reaction-enabled steady-state CFD simulation results with that obtained by simulating the compartment model as a flow sheet in the Aspen Plus simulator. In that work, we performed the exercise for the case of cavity under isothermal conditions. In the present work, a similar exercise is performed for the cavity under nonisothermal condition, by considering the homogeneous water-gas shift reaction (eq 12), described by a second-order rate expression (eqs 13)–15) taking place in the cavity. Reaction enabled CFD simulations are performed in order to obtain the product gas composition at the outlet under similar boundary conditions (i.e., for a chosen case of feed flow rate = 226.28 m³/h, feed temperature = 873 K, the nonspalling case, and vertical injection) mentioned in section 2, in addition to the reactive conditions. The feed composition used and convergence criteria can be found elsewhere.⁸

Water-Gas Shift Reaction:



$$R = (k_f C_{\text{CO}} C_{\text{H}_2\text{O}}) - (k_b C_{\text{CO}_2} C_{\text{H}_2}) \quad (13)$$

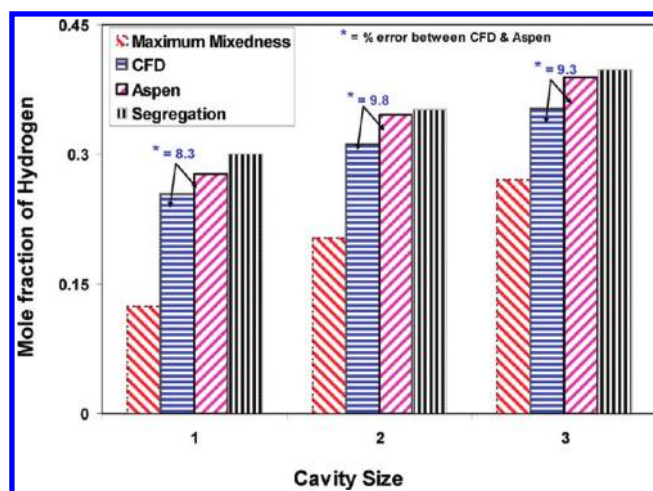


Figure 14. Comparison of mole fraction of H₂, which is obtained from all the models (CFD, Aspen, Segregation, Maximum mixedness) for all of the cavity sizes.

where

$$k_f = 2.78 \times \exp\left(\frac{-12600\text{kJ/kgmol}}{RT}\right) \quad (14)$$

$$k_b = 104.91 \times \exp\left(\frac{-78400\text{kJ/kgmol}}{RT}\right) \quad (15)$$

Table 6. Operating Conditions for Both Aspen and Reaction-Enabled CFD Simulations

operating parameter	Cavity Size		
	1	2	3
T_{av} (for Aspen simulations)	984 K	958 K	951 K
velocity	4 m/s	4 m/s	4 m/s
feed mixture (at 873 K) at inlet	CO + H ₂ O	CO + H ₂ O	CO + H ₂ O
feed composition at inlet	equal mole fraction	equal mole fraction	equal mole fraction

The reaction kinetics is obtained from Perkins and Sahajwalla.²² After solving for the steady state in the cavity, the area-weighted average of the mole fractions of product species at the outlet were calculated for all three cavity sizes. The computational time required to obtain the steady-state composition from a reaction-enabled simulation is 500–600 CPU h on a Pentium Core 2 Duo 2.67 GHz workstation. The mole fraction of H₂ at the outlet is calculated for all the cavity sizes and is shown in Figure 14.

Next, the corresponding compartment model (see Figure 3 and Table 2) (i.e. the reactor network) is simulated as a flow sheet in an ASPEN PLUS steady-state flow sheet simulator. The model parameters (i.e., the bypass ratio and the individual volumes of all reactors in the compartment model) are assigned to the blocks in the flow sheet. For simplicity, it is assumed that the temperature of each reactor in the compartment model is same as the volume-weighted average temperature (T_{av}) of the cavity, as calculated by eq 16.

$$\exp\left(\frac{-E_{act}}{RT_{av}}\right) = \frac{\sum_{i=1}^n V_i \exp\left(\frac{-E_{act}}{RT_i}\right)}{\sum_{i=1}^n V_i} \quad (16)$$

where i is the total number of cells in the cavity grid ($i = 1, \dots, n$); T_i and V_i are the respective temperature and volume of the i th cell in the cavity grid; and R and E_{act} are the respective universal gas constant and activation energy of a chosen reaction.

T_{av} values are calculated for both forward and backward reactions using the activation energies of the corresponding reactions. The difference between these temperatures is <10 °C. The arithmetic average of these two temperatures is considered as the temperature of each reactor in the compartment model (see Table 6). Steady-state simulations were performed in order to determine the product gas compositions from this network of ideal flow reactors, i.e., the compartment model. The computational time needed to simulate the compartment model in ASPEN simulator is <5 min, which is an order of magnitude lower than that with the reaction-enabled CFD approach. The compositions of H₂ or CO₂ in the outlet gas, obtained from ASPEN simulations, are compared with that of the reaction-enabled CFD predictions in Figure 14. It can be seen that both the predictions agree reasonably well. We have also predicted the conversions by considering the two extreme levels of micromixing, i.e., using the maximum mixedness model and the complete segregation model based on the respective E -curves. The procedure to calculate the conversions from these models may be found in standard textbooks.³² These simple models are expected to provide bounds on conversions, for a given RTD, as observed from the results shown in Figure 14. The proposed procedure of compartment modeling thus provides a less computationally intensive and yet reliable method to predict

product gas compositions in UCG at a particular time for a given size and shape of cavity.

7. CONCLUSIONS

The impact of nonisothermal conditions on the reactant gas flow patterns in a UCG cavity has been analyzed in this work. Several possible scenarios are explored. When spalling occurs in the UCG cavity, the heterogeneous coal reactions may take place on the floor of the cavity, or in the entire cavity volume. On the other hand, when the coal does not have a tendency to spall, the reactions would occur on the roof of the cavity. Thus, in the two cases of spalling and nonspalling, the temperature profiles inside the UCG cavity are different. Consequently, the reactant gas flow patterns are also strongly affected.

Using CFD and compartment modeling techniques, we demonstrate here that radiation dominates over buoyancy-driven flow when coal combustion takes place at the roof of the cavity (i.e., in the absence of spalling). On the other hand, for the spalling case, when the coal reactions take place on the floor of the cavity, buoyancy-driven convective currents were found to strongly govern the velocity and temperature fields. Simplified modeling strategies for the characterization of the flow patterns for these two cases are proposed and validated here, when the feed temperature is sufficiently high. These strategies are demonstrated to result in significant computational savings, and they also provide the direction for further process modeling of the complex UCG process.

The effect of changing various operating and design parameters such as the feed temperature, flow rate, and orientation of the inlet nozzle, on the flow patterns are also studied in detail here. Finally, the proposed compartment model is used to predict outlet conversions for a homogeneous water-gas shift reaction occurring in the cavity. The predicted conversion is found to agree well with that obtained using reaction-enabled CFD simulations, thus validating the simplified compartment modeling approach presented here, for nonisothermal conditions. The results provide good insight into the cavity flow patterns under different practically relevant conditions of UCG and also provide a solid platform for further work on simplified phenomenological models for UCG.

AUTHOR INFORMATION

Corresponding Author

*Tel.: (022) 2576 7295. Fax: (022) 2572 6895. E-mail: preeti@iitm.ac.in.

NOMENCLATURE

ρ = density, kg/m³

t = time, s

\vec{v} = velocity tensor
 p = static pressure
 $\vec{\tau}$ = stress tensor
 $\rho\vec{g}$ = gravitational body force
 F = external body force
 J_j = diffusion flux of species j
 Y_i = mole fraction of species i
 V_0 = volumetric flow rate, m^3/s
 B = bypass ratio
 V_{Mj} = volume of the j th continuously stirred tank reactor (CSTR) in the main stream of the compartment model, m^3
 V_{Bj} = volume of the j th CSTR in the side stream of the compartment model, m^3
 V_P = volume of plug flow reactor in the compartment model, m^3
 τ_{mj} = residence time of the j th CSTR in main stream, s
 τ_{bj} = residence time of the j th CSTR in bypass stream, s
 τ_e = residence time of the plug-flow reactor at the exit, s
 dC_{mji} = derivative of tracer concentration of the j th CSTR in the main stream for the i th iteration
 dC_{bji} = derivative of tracer concentration of the j th CSTR in the bypass stream for the i th iteration
 C_{mji} = tracer concentration in the j th CSTR in the main stream for the i th iteration
 C_{bji} = tracer concentration in the j th CSTR in the bypass stream for the i th iteration
 h = time step size
 e = average percentage error
 F_L = forward length (i.e., cavity growth in forward direction), cm
 B_L = backward length (i.e., cavity growth in backward direction), cm
 W = width of the cavity (i.e., cavity growth in transverse direction), cm
 H = height of the cavity (i.e., cavity growth in vertical direction), cm
 k_{eff} = effective thermal conductivity
 J_j = diffusion flux of species j
 R_i = rate of reaction species j
 k_f = forward reaction rate constant
 k_b = backward reaction rate constant
 A = frequency factor
 E_f = activation energy for forward reaction
 E_b = activation energy for backward reaction
 C_i = concentration of species i
 VI = vertical injection
 II = inclined injection
 HI = horizontal injection
 RHT = roof at high temperature
 BHT = bottom at high temperature
 $SP\text{-}BHT$ = bottom at high temperature with spalled particles

REFERENCES

- (1) <http://www.worldcoal.org/resources/coal-statistics> (accessed on October 15, 2010).
- (2) BP Statistical Review of World Energy—2009. Technical Report. BP plc, Global, London, U.K., 2010.
- (3) Khadse, A.; Qayyumi, M.; Mahajani, S. M.; Aghalayam, P. Underground Coal Gasification: A New Clean Coal Utilization Technique for India. *Energy* **2007**, *32*, 2061–2071.
- (4) Green, M. B.; Rippon, B. Underground coal gasification in deep coal seams with carbon capture and storage. Presented at the 22nd Pittsburgh Coal Conference, Pittsburgh, PA, September 2005.
- (5) Gregg, D. W.; Edgar, T. F. Underground Coal Gasification. *AIChE J.* **1978**, *24*, 753–781.
- (6) Daggupati, S.; Mandapati, R. N.; Mahajani, S. M.; Ganesh, A.; Mathur, D. K.; Sharma, R. K.; Aghalayam, P. Laboratory Studies on Combustion Cavity Growth in Lignite Coal Blocks in the Context of Underground Coal Gasification. *Energy* **2010**, *35* (6), 2374–2386.
- (7) Daggupati, S.; Mandapati, R. N.; Mahajani, S. M.; Ganesh, A.; Mathur, D. K.; Sharma, R. K.; Aghalayam, P.; Laboratory Studies on Cavity Growth and Product Gas Composition in the context of Underground Coal Gasification. *Energy* **2011**, DOI:10.1016/j.energy.2010.12.051.
- (8) Daggupati, S.; Mandapati, R. N.; Mahajani, S. M.; Ganesh, A.; Mathur, D. K.; Sharma, R. K.; Aghalayam, P. Compartment modeling for flow characterization of underground coal gasification (UCG) cavity. *Ind. Eng. Chem. Res.* **2010**, *50*, 277.
- (9) Burton, E.; Friedmann, J.; Upadhye, R. *Best Practices in Underground Coal Gasification*; Contract No. W-7405-Eng-48: U.S. DOE, Lawrence Livermore National Laboratory: Livermore, CA, 2006.
- (10) Shafirovich, E.; Varma, A. Underground Coal Gasification: A Brief Review of Current Status. *Ind. Eng. Chem. Res.* **2009**, *48*, 7865–7875.
- (11) Aghalayam, P. *Underground Coal Gasification: A Clean Coal Technology, Hand Book of Combustion*; Wiley-VCH: Chichester, U.K., 2010; Vol. 5, pp 257–275.
- (12) Khadse, A.; Qayyumi, M.; Mahajani, S. M.; Aghalayam, P. Reactor Model for the Underground Coal Gasification (UCG) Channel. *Int. J. Chem. Reactor Eng.* **2006**, *4*, A37.
- (13) Yang, L. Study on the Model Experiment and Numerical Simulation for Underground Coal Gasification. *Fuel* **2004**, *83*, 573–584.
- (14) Thorsness, C. B.; Kang, S. W. *Further Devolvement of General-Purpose, Packed-Bed Model for Analysis of Underground Coal Gasification Processes*. Report No. UCRL-92489, U.S. DOE, Lawrence Livermore National Laboratory: Livermore, CA, 1985.
- (15) Thorsness, C. B.; Greens, E. A.; Sherwood, A. A. *One Dimensional Model for In-Situ Coal Gasification*. Report No. UCRL-S2523, U.S. DOE, Lawrence Livermore National Laboratory: Livermore, CA, 1978.
- (16) Magnani, C. F.; Farouq, A. S. M. Mathematical Modeling of the Stream Method of Underground Coal Gasification. *Soc. Petrol. Eng. J.* **1975**, *15*, 425.
- (17) Dinsmoor, B.; Galland, J. M.; Edgar, T. F. The Mechanism of Channel Growth During Underground Coal Gasification. *J. Petrochem. Technol.* **1978**, 695.
- (18) Harloff, G. J. Underground Coal Gasification Cavity Growth Model. *J. Energy* **1983**, *7*, 410–415.
- (19) Park, K. Y.; Edgar, T. F. Modeling of Early Cavity Growth for Underground Coal Gasification. *Ind. Eng. Chem. Res.* **1987**, *26*, 237–327.
- (20) Yang, L.; Liu, S. Numerical Simulation on Heat and Mass Transfer in Process of Underground Coal Gasification. *Numer. Heat Transfer, Part A* **2003**, *44*, 537–557.
- (21) Perkins, G.; Sahajwalla, V. A Mathematical Model for the Chemical Reaction of a Semi-Infinite Block of Coal in Underground Coal Gasification. *Energy Fuels* **2005**, *19*, 1679–1692.
- (22) Perkins, G.; Sahajwalla, V. Steady-State Model for Estimating Gas Production from Underground Coal Gasification. *Energy Fuels* **2008**, *22*, 3902–3914.
- (23) Britten, J. A.; Thorsness, C. B. A Model for Cavity Growth and Resource Recovery During Underground Coal Gasification. *In-situ* **1989**, *13*, 1–53.
- (24) Perkins, G.; Sahajwalla, V. A Numerical Study of the Effects of Operating Conditions and Coal Properties on Cavity Growth in Underground Coal Gasification. *Energy Fuels* **2006**, *20*, 596–608.
- (25) Cena, R. J.; Thorsness, C. B. Underground coal gasification data base. Report No. UCID-19169, U.S. DOE, Lawrence Livermore National Laboratory: Livermore, CA, 1981.
- (26) Yonggang, L. U. O.; Margaretha, C.; Stephen, D. Comparison of UCG cavity growth with CFD model predictions. Presented at the 7th International Conference on CFD in the Minerals and Process Industries CSIRO, Melbourne, Australia, December 9–11, 2009.

(27) Shih, T.-H.; Liou, W. W.; Shabbir, A.; Yang, Z.; Zhu, J. A new $k-\varepsilon$ eddy viscosity model for high Reynolds number turbulent flows. *Comput. Fluids* **1995**, *24* (3), 227.

(28) FLUENT 6.3, *Users Guide*. Fluent, Inc.: Lebanon, NH, December 2005.

(29) Sazhin, S. S.; Sazhina, E. M.; Saravelou, O. F.; Wild, P. The P-1 model for the thermal radiation transfer: Advantages and limitations. *Fuel* **1996**, *75* (3), 289.

(30) Kuyper, R. A.; Van Deer Meer, H.; Hoogendoorn, C. J. Turbulent natural convection flow due to combined buoyancy forces during underground gasification of thin coal layers. *Chem. Eng. Sci.* **1994**, *49* (6), 851–861.

(31) Perkins, G.; Sahajwalla, V. Modeling of heat and mass transport phenomena and chemical reaction in underground coal gasification. *Chem. Eng. Res. Des.* **2007**, *85* (A3), 329–343.

(32) Fogler, H. S. *Elements of Chemical Reaction Engineering*; Prentice Hall PTR: Upper Saddle River, NJ, 1999.